Acoustic Intensity in Military Jet Noise Field Characterization

Trevor A. Stout

A senior thesis submitted to the faculty of
Brigham Young University
in partial fulfillment of the requirements for the degree of

Bachelor of Science

Kent Gee and Tracianne Neilsen, Advisors

Department of Physics and Astronomy

Brigham Young University

[August] 2013

ABSTRACT

Acoustic Intensity in Military Jet Noise Field Characterization

Trevor A. Stout
Department of Physics and Astronomy
Bachelor of Science

Acoustic intensity measurements of the F-22A Raptor are analyzed as part of ongoing efforts to characterize the noise radiation from military jet aircraft. Data were recorded from a rig of microphones and an attached tetrahedral intensity probe at various locations to the sideline and aft of the aircraft. Numerical analysis of the intensity at one-third octave band center frequencies along various measurement planes and at a 23 m radius arc reveals the magnitude and directionality of the vector acoustic intensity. Differences in the trends for low-frequency and high-frequency data are discussed and, via a simple ray tracing method from maximum intensity regions, interpreted in terms of far-field behavior and source location. In particular, the extended source region contracts and moves upstream with increasing frequency, and vector directionalities point farther toward the sideline.

Keywords: acoustic intensity, military jet, jet noise

ACKNOWLEDGMENTS

[I would like to acknowledge the continuing, tireless efforts of my academic advisors, Dr. Kent Gee and Dr. Tracianne Neilsen, and also the invaluable assistance from other members of the Brigham Young University jet noise research team, especially Alan Wall. I also thank the Office of Naval Research for their funding, and the Department of Physics and Astronomy for this opportunity.]

Contents

List of Figures

Chapter 1

Introduction

1.1 Motivation

Currently, there is significant interest in the behavior of sound from military jet engines. This sound contributes significantly to hearing loss in Air Force personnel and to general noise pollution. Because of the importance of jet sound, a host of the scientific community including theorists and engineers has been involved in an effort to better understand and characterize jet noise, using many different techniques. Studies of the jet plume, (the column of turbulent fluid flow ejected by the engine), offer insights about propagation of sound and the nature of the source, such as where a given frequency of sound comes from, and in what direction it travels away from the jet.

Because of the difficulty of obtaining information directly from the turbulent flow from high-temperature, supersonic, full-scale jet engines, most methods use arrays of microphones outside the jet plume. The number and placement of the microphones varies, based on what is optimal for a given analysis technique. For example, acoustical holography requires a closely-spaced grid of microphones over a large region near the noise source in order to make precise calculations. In contrast, to make an approximation of three-dimensional acoustic intensity at a point, only the

pressure measurements from four closely-spaced microphones are required. Techniques such as beamforming [1] [2], acoustical holography [2] [3] [4], and equivalent source methods [5] [6] have been applied previously in characterizing jet noise sources. The Brigham Young University (BYU) Acoustics Research Group (ARG) working on this project has already applied these and other methods. In this thesis, I describe the study of acoustic intensity in jet noise. Application of multiple techniques often validates previous results, solidifying theories of jet noise characteristics.

The acoustic intensity, or vector intensity, is an important quantity in acoustics. As opposed to the aforementioned techniques, it has not been heavily applied by the scientific community to the jet noise characterization effort. It is a measure of the sound radiation energy flow through an area (in SI units W/m^2). Typically, the intensity is calculated in a narrowband frequency spectrum, giving frequency-dependent information about the energy flow vector (including magnitude and direction). Using multiple data points around a noise source, it is possible to construct maps of the energy flow, and these vectors can be extrapolated to estimate near-field (near to the source compared to a wavelength) and far-field (many wavelengths away from the source) propagation and source characteristics.

We report on our effort to expand the study of acoustic intensity from military jets. Previous notable studies of jet acoustic intensity are rare, and often use data from flows which are laboratory scale, and limited in temperature and velocity (conditions significant in a full-scale jet plume). Ventakesh, et al. [1], used a one-dimensional intensity probe to validate the application of beamforming techniques in the analysis of a subsonic jet. The probe was two microphones which took simultaneous pressure measurements in a line. These measurements were then processed to approximate the intensity in the direction connecting the two microphones (this technique is elaborated in Chapter 2). Laufer, et al. [7], used a directional microphone attached to a spherical reflector to obtain directional measurements from a supersonic jet with mach numbers 1.5 to 2.5. The work of Jaeger and Allen [8], who used a two-dimensional intensity probe (using four

microphones in order to approximate the intensity in two dimensions at a time) in characterizing Mach 0.2-0.6 jets, represents one of the most in-depth applications. However, their initial work differs significantly from high-amplitude jet conditions like those from military aircraft and resulting source characteristics.

Recently, an ARG team conducted near-field investigations of solid rocket motor plume acoustics, including acoustic intensity analysis using a three-dimensional intensity probe [9] [10] [11]. We also used this probe in the jet noise study which is the focus of this thesis. By analyzing the pressure measurements taken by the probe, I constructed vector maps of the sound energy flow of an F-22 Raptor, and then used these maps to say something about the source location and directionality. In general, I found that high-frequency sound tends to originate from farther upstream (closer to the jet nozzle) in the jet plume, and that it propagates in a direction closer to the jet sideline. These trends were expected based on previous analysis methods, although the intensity analysis presented here does not always agree with other methods on the specific source location or directionality.

1.2 Experimental setup

Researchers at Blue Ridge Research and Consulting and BYU ARG used the intensity probe to record data during extensive acoustic measurements of the noise field of a Lockheed Martin/Boeing F-22A Raptor (F-22) [12] [13]. The F-22 was tethered down in the center of an 80 ft wide concrete run-up pad surrounded on both sides by rain-packed dirt (see Fig. 1.1). One engine was held at idle while the pilot fired the other, cycling through four different engine conditions chosen to give a wide range in thrust conditions: afterburner (full throttle with additional fuel injection), military (full throttle), intermediate (80% throttle), and idle. For each engine condition, held as constant as possible, microphones recorded data at a multitude of prescribed locations. In order to minimize

Figure 1.1 The tethered F-22 with one active engine. The microphone rig is also visible.

Figure 1.2 90-microphone rig with attached 4-microphone intensity probe.

reflection interference, we placed the microphones as far as possible from obstacles such as a blast deflector 24.4 m behind the jet, and a short wall nearly parallel to the jet centerline (the line running parallel to the center of the jet plume) and 30 m to the side. Reflection interference occurs when sound waves reflect off of surfaces, causing indirect pressure waves to be recorded at the microphone location. These obstacles were structures with hard surfaces already in the vicinity of the run-up pad, which could not be removed. We monitored meteorological quantities such as temperature fluctuations and wind speeds during the measurements and determined their effects to be minor for the duration of the experiment.

The three-dimensional intensity probe (which was used in the previous rocket study) was at-

tached to the top of a 90-microphone rig which recorded the data at several locations along three near-field measurement planes (corresponding to straight lines in the horizontal plane along the ground) using guide rails and along a 23-m radius arc centered 5.5 m downstream from the nozzle exit of the active engine (see Figs. 1.2 and 1.3). Two of the near-field measurement planes, numbers 1 and 2, were positioned parallel to the estimated shear layer of the jet plume, the edge of the turbulence caused by mixing of the high-velocity jet plume with ambient air. The third plane ran parallel to the centerline. With the rig positioned at a point along one of these planes, the pilot fired the engine at one condition, after which the rig was moved to the next point and the process repeated. Measurements were made with the array at several locations and heights in 2.4 m horizontal increments along the measurement planes and 10 degree increments along the arc, with the probe recording data at each of these locations (each individual measurement period is referred to as a 'scan'). The rig took so many measurements primarily to aid in holography calculations, but the data the probe recorded at the same locations are the primary focus of this thesis.

In addition, a fixed array of 50 microphones was placed along the ground 11.6 m from the jet centerline, which provided reference levels between the various measurement scans (see "reference microphones" in Fig. 1.3). In processing the pressure measurements, the levels from this reference array were used as a baseline in order to address differences in overall magnitudes. In other words, the reference array helped to "smooth" out some of the variation due to human error in between scans.

For idle, intermediate, and military engine conditions, the microphones took data at a sampling rate of 96 kHz. This corresponds to a Nyquist frequency limit, the high-frequency limit up to which frequency content of the sound can be reliably calculated, of 48 kHz. For the afterburner condition, the microphones took data at 48 kHz, which reduced the data storage requirements for that condition.

The intensity probe was constructed as an inverted (tip pointing to ground) tetrahedron frame

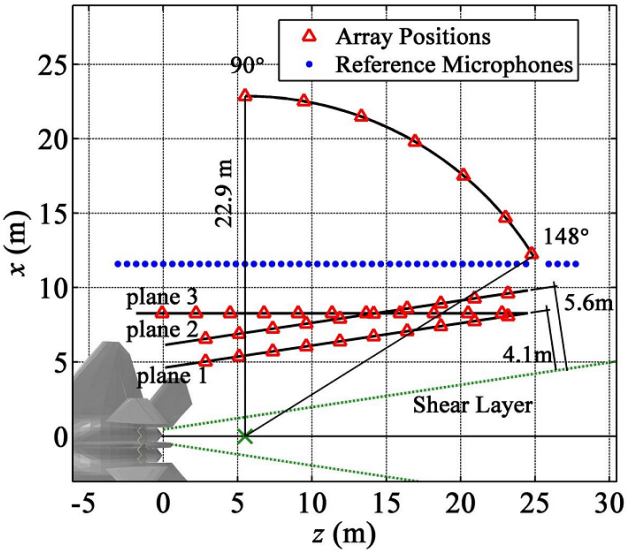

Figure 1.3 Measurement planes and locations where intensity data was acquired. The jet is rendered with the active engine at the origin.

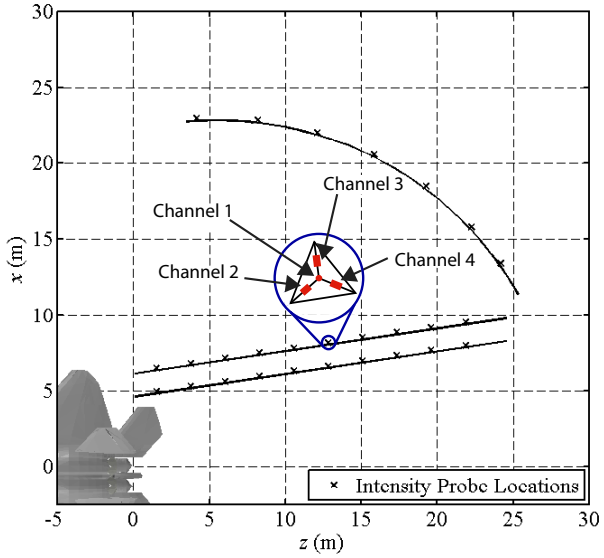

Figure 1.4 Orientation of intensity probe microphones. Note that the two-dimensional representation of the tetrahedron is not to scale.

with microphones mounted at the vertices, pointing inwards. The microphones were phase-matched to improve the accuracy of the intensity calculations, as explained in Chapter 2. The intensity probe was positioned so that two microphones were aligned parallel to the measurement array guide rail (see Fig. 1.4). In this thesis, I denote the centerline of the plume the z-axis, and the orthogonal horizontal direction the x-axis. The origin of the coordinate axes is the end of the active jet nozzle. The height of the probe was near the center height of the jet nozzle for all the data considered hereafter, so the relatively small y-component (vertical) of the intensity is not presented.

1.3 Overview

I used the data from these microphones to construct intensity approximations via the analysis methods in Chapter 2. In short, the intensity estimate using two microphones provided an estimate of the vector portion along the axis connecting the two microphones, so that the multi-axial tetrahedral setup, after some data processing, provided three-dimensional vector information. Using multiple data locations, I mapped out the field of acoustic energy flow in the region surrounding the jet plume.

In this thesis, I analyze the intensity directionality and source location as a function of frequency. In Chapter 2, I provide an introduction to acoustic intensity and describe the method and approximations in the intensity calculations. I also discuss the verification and limitations of the data and describe the methods for far-field and source characterization. In chapter 3, I present multiple vector maps for select frequencies.

The maps show trends in low to high-frequency directionalities and source locations, which I discuss and analyze according to the methodology in Chapter 2. The most important trend found through the maps is that the generalized source location contracts and moves upstream for higher frequency. Also, the generalized direction of maximum energy flow points closer to the jet sideline

for increasing frequency.

Chapter 2

Data analysis

2.1 Overview of intensity

Every source of sound radiates energy with some level of power, the rate at which the source outputs energy. A common method for analyzing a source of sound is to measure its sound power. Microphones are placed around the source to measure the pressure levels, from which the sound power is extrapolated. However, this measurement gives no information about the direction of this sound radiation. Since we are interested in the direction of the sound energy output by the jet plume from the F-22 engine, we must instead calculate the intensity. Calculation of sound intensity at a given point is a measurement of the energy flow, including magnitude and direction at the point. The magnitude of the intensity describes how much sound power crosses a unit area normal to the direction of propagation. The SI units of intensity are Watts per meter squared, and since it contains directional information, it is a vector quantity.

Energy is transferred by a propagating sound wave when one element of the fluid (air in our case) does work on an adjacent element. The rate at which this work is done per unit area is given

by,

$$\mathbf{I}(t) = p(t)\mathbf{u}(t), \tag{2.1}$$

where $\mathbf{I}(t)$ denotes the vector intensity as a function of time, $p(t)$ the scalar pressure and $\mathbf{u}(t)$ the vector particle velocity. The bolded symbols denote vector quantities. The particle velocity can vary as rapidly as the pressure wave which alternately pushes and pulls the fluid. To get a better overall picture of the net intensity, in practice the time-averaged intensity is desired, so the right-hand side is integrated over the time length of the measurements:

$$\mathbf{I} = \frac{1}{T}\int_0^T p(t)\mathbf{u}(t)\,dt. \tag{2.2}$$

For the F-22 measurements, the full time length used for integration is about $T = 25$ s, which differs depending on the actual measurement time. The scalar pressure $p(t)$ used in the above formulae is measured using an ordinary type of microphone in the sound field. The vector particle velocity is not the velocity of a single molecule of air but is the overall velocity of a small volume of the fluid in the sound field, which moves back and forth in response to the sound pressure waves. The particle velocity describes the net velocity of this small volume of fluid. Both quantities are needed for an intensity calculation, but the particle velocity is much more difficult to measure directly with precision, requiring special velocity probes.

2.1.1 Finite difference

The particle velocity can instead be approximated indirectly through an application of Euler's equation, a form of Newton's second law for inviscid fluids. Euler's equation,

$$\rho_0 \frac{d\mathbf{u}(t)}{dt} = -\bigtriangledown p(t), \tag{2.3}$$

describes the change in particle velocity in the fluid with equilibrium density ρ_0, relating it to the gradient of the pressure, $\bigtriangledown p$. The particle velocity in one direction–e.g., the x-direction–is found

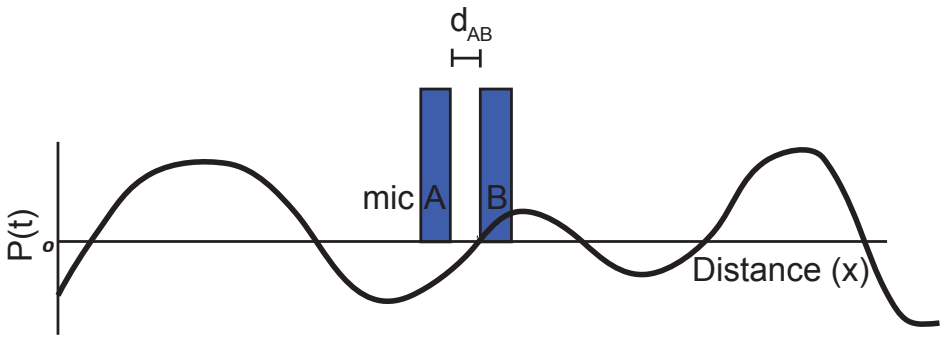

Figure 2.1 Two closely-spaced microphones take simultaneous measurements of the pressure curve, which measurements are used in the finite difference approximation method. The distance between the two microphones is also an important constant.

by rearranging and integrating:

$$u_x = -\frac{1}{\rho_0}\int_0^T \frac{dp(t)}{dx}\,dt. \tag{2.4}$$

To find the gradient of the pressure in this direction, we use the finite difference approximation which requires the pressure data acquired by as few as two microphones. The pressure at one microphone (microphone B) is subtracted by the pressure at the other (microphone A), and the result divided by the distance between the microphones:

$$(\bigtriangledown p)_x \approx \frac{p_B - p_A}{d_{AB}}. \tag{2.5}$$

This gives an approximation of the derivative of the pressure curve in one dimension centered at the point half-way between the two microphones.

Since we are interested in the intensity for a given frequency, we first take the fast Fourier transform (FFT) of the pressure signals. The FFT of the raw pressure data returns the spectrum, ($X_A(\omega)$, for the pressure signal from microphone A), given by

$$X_A(\omega) = \int_{-\infty}^{\infty} \mathbf{u}(t)e^{i\omega t}\,dt, \tag{2.6}$$

where i is the imaginary number, and ω is the frequency. Note that the spectrum $X_A(\omega)$ has frequency, not time, as its argument.

In the frequency domain, the imaginary part of the cross spectrum between two pressure signals, $\Im\{G_{AB}\}$, contains the necessary information about the pressure gradient approximation. The cross spectrum, combining two spectra, is given in the usual way by

$$G_{AB} = X_A^* \cdot X_B. \tag{2.7}$$

Finally, the intensity in the direction along the two microphones and centered between them is given by [14]:

$$\mathbf{I} = \frac{-1}{\rho_0 \omega d_{AB}} \Im\{G_{AB}\}. \tag{2.8}$$

This formulation is mathematically equivalent to the finite difference method shown in the time domain. Because the data we took was from a static engine firing, we time-averaged this quantity over the full length of time, about 25 seconds, to improve precision.

2.1.2 Intensity in three dimensions

In order to gain a three-dimensional picture of the intensity directionality, microphones must be placed so as to give intensity results pointing along each dimension. In our study, we used a tetrahedral probe with four microphones (see Fig. 2.2), one at each vertex, giving some data in the three coordinate directions. Once we calculated the intensities along each of the four sides of the tetrahedron, we applied weightings to each component according to a least-squares technique developed by Pascal and Li [15] to calculate the three-dimensional overall approximate intensity centered at the geometric center of the tetrahedron. Using the numbering system shown in Fig. 2.2, the intensity components in the cardinal directions are given by [16],

$$I_x = \frac{1}{32\rho_0 \omega a}(\sqrt{2} \cdot \Im\{-G_{12} + 2G_{13} - G14 + 3G_{23} - 3G_{34}\}) \tag{2.9}$$

$$I_y = \frac{1}{32\rho_0 \omega a}(\sqrt{6} \cdot \Im\{G_{12} - G14 - G_{23} - 2G24 - G_{34}\}) \tag{2.10}$$

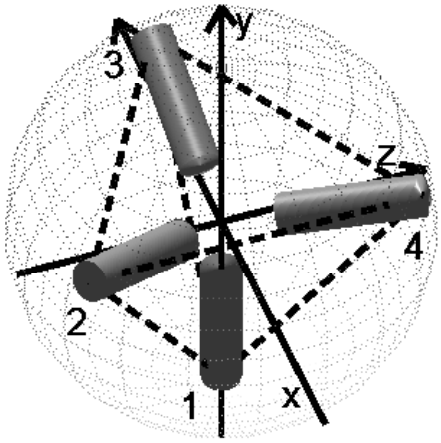

Figure 2.2 The placement and orientation of the four probe microphones is shown. Note how the axis connecting mics 2 and 4 is parallel to the z axis. Image courtesy of Michael Muhlestein.

$$I_z = \frac{1}{32\rho_0\omega a}(4 \cdot \Im\{G_{12} + G_{13} + G14\}), \tag{2.11}$$

where a is the distance from each microphone to the geometric center of the tetrahedron (this distance is the same for all the microphones).

The tetrahedral probe recorded data for the duration of each scan, along all four measurement planes and for each engine condition, so that the calculations gave us multiple vector data points to make intensity maps, which are detailed in Chapter 3.

2.1.3 Limitations of the finite difference intensity method

Some limitations inherent in the two-microphone approximation method include errors in low-frequency calculations due to phase mismatch, and in the high-frequency range due to scattering effects and error in the finite-difference approximation [14]. Microphones measure the phase of an acoustic signal differently due to the differing resonant frequencies and damping from the microphones' construction [17]. When the spacing between two microphones is small, this electronic phase difference becomes important in comparison to the low-frequency acoustic phase difference

which occurs geometrically (see Fig. 2.1 for an example of how geometric distance might affect acoustic phase). Thus, the electronic phase difference introduces uncertainty or error into the calculation of intensity, and must be considered. In calibrating microphones for use in an intensity probe, the phases should be matched as closely as possible.

In our case, we restricted our analysis to the 100 Hz to 4 kHz range, because this showed the most consistency in results between microphones. A more detailed explanation of this choice in frequency range is found in the next section.

2.2 Data validation

We analyzed the data from the intensity probe microphones in two different ways to ensure good calibration and reliability. Good calibration is important when comparing the cross-spectra of microphones, since a relative under or oversensitivity of a microphone will shift the finite difference approximation. Specifically, we compared the intensity probe microphone power spectral densities (PSDs), and tested their time waveforms (raw pressure data) for calibration precision. By looking at the overall shapes and the agreement of the PSDs and time waveforms, we determined that the microphone sensitivity calibration was good enough for our approximations, as shall be explained in this section.

The PSD is a decomposition of the mean squared pressure of a signal as a function of frequency. The PSDs for well-calibrated microphones lie close to each other and have the same shape, i.e. the frequency content of the signal picked up by each microphone is roughly the same, to within $\pm$ 2 dB. In analyzing the PSDs for the four probe microphones, we paid special attention to the 100 Hz to 4kHz range [18], in which we decided to restrict our intensity approximations. For a large portion of frequencies, the PSDs of the four probe microphones agreed within the acceptable bounds. See Fig. 2.3 for an example PSD comparison at plane 1, scan 5 for afterburner engine

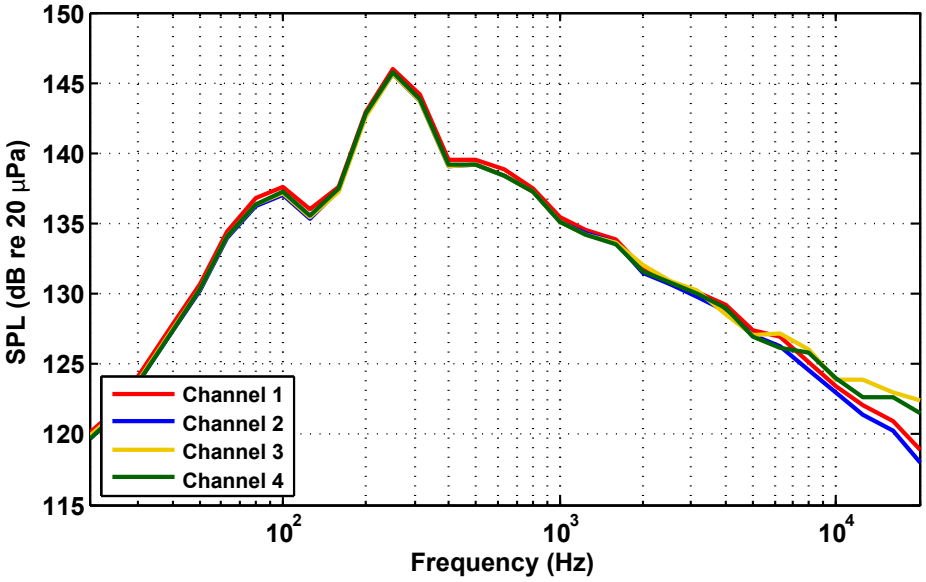

Figure 2.3 Power spectral densities smoothed to one-third-octaves of the four microphones at plane 1, scan 5, afterburner condition.

condition.

Above about 4 kHz, the PSD agreement starts to break down. This is caused by scattering effects due to the tetrahedral external frame and bodies of the microphones and because the microphones were not all oriented at normal incidence to the sound propagation. The angle at which the sound is incident on the microphone face determines the amount of scattering. The orientation of the microphones was dictated by the framework of the tetrahedral intensity probe, with each microphone facing a different direction (see Fig. 2.2). Thus, with increasing frequency the scattering effects would tend to split the PSDs. As is seen in the PSD plots, however, this effect is not significant in the frequency range used for our intensity approximations.

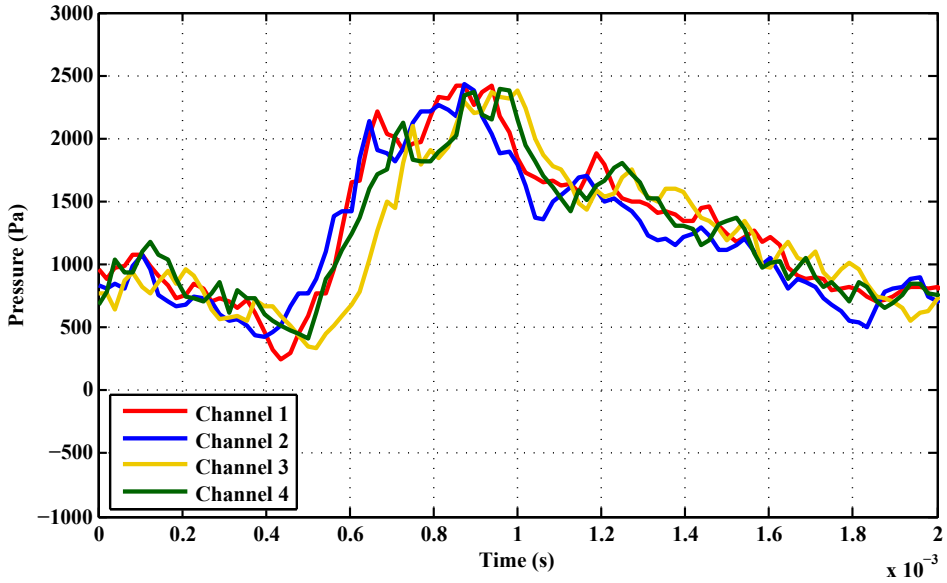

Figure 2.4 Time waveforms of the four intensity probe microphones. Note how signals arrive at the different microphones sequentially based on their relative locations.

2.2.1 Time waveforms

We also inspected samples of the time waveforms from the four microphones to further validate the calibration. Because of the close proximity of the microphones, we expected that the waveforms should be similar, but offset slightly in the time domain, according to the time required for sound to propagate to each microphone location. As can be seen in Fig. 2.4, microphone 1 received sound information slightly before microphone 2, followed by 3 and then 4. Were we to shift the waveforms by certain small amounts of time, they would lie nearly on top of each other. The best way to see the order in which the microphones received information is by examining where the pressure value suddenly spikes or drops, which corresponds to a pressure shock reaching the probe (see $t = .6$ ms in Fig. 2.4)).

This ordering was what we expected, since other acoustic methods anticipated the generalized source region to center around 5.5 m downstream in the jet plume. A ray traced directly from this estimated source to this particular probe location reaches probe 1 first, then 2, 3 and 4. At different

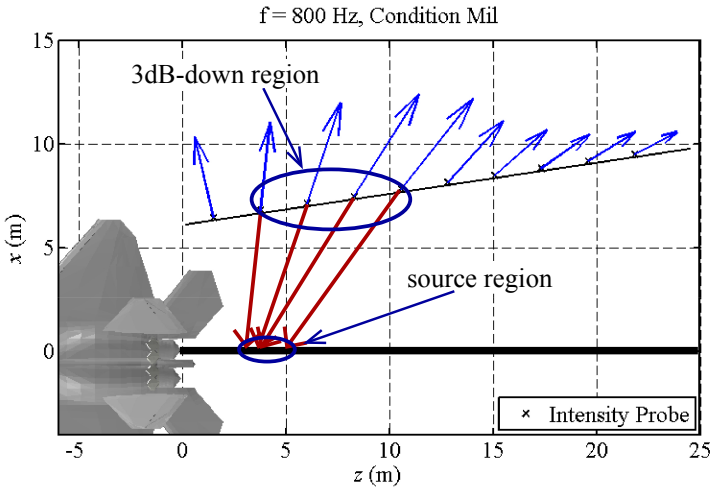

Figure 2.5 Process of tracing vectors from a 3dB-down region to the jet centerline. The jet centerline corresponds to the active engine during the run-up tests.

locations, the waveform time offsets behaved in the same manner, just with a different geometry.

2.3 Directionality and source characterization method

After calculating the intensity vectors for all of the data locations indicated in Fig. 1.3 and for multiple frequencies, we used these results to determine the direction of energy flow and the source locations. We looked at the direction of the intensity vectors with the largest magnitudes, tracing the vectors back towards the jet plume. Because the point of maximum intensity indicates the area of greatest energy flow, this ray-tracing technique provides an estimation of source location or far-field directivity (as illustrated in Fig. 2.5). Because of the effects of ground reflections and variations in the run-up tests, which may have changed precisely which data point had the maximum magnitude for a given measurement plane, we chose to look at a region of high intensity at each measurement plane called the "3dB-down region." Specifically, we included the data point of maximum magnitude and each data point within 3 dB from maximum. We chose this number because it gave a manageable region of included data points, and helped to overcome these data-

skewing effects.

After calculating the 3dB-down region, we traced the intensity vectors in the measurement plane directly back to the jet centerline and used the positions of the intersections to describe the approximate source location region. (See Fig. 2.5 for an example of how the vectors were traced back.) These results are presented in the next chapter.

Chapter 3

Results and discussion

3.1 Intensity maps

Using the methodology described in Chapter 2, we created multiple intensity maps at different frequencies to show the characteristic low-to-high frequency trends in direction and magnitude. Figures 3.1(a) through 3.4(b) display maps for all four engine conditions, at indicated narrow-bin frequencies. (These frequencies correspond to preferred one-third octave band center frequencies to facilitate comparisons with other data sets.) Only the data from measurement planes 1, 2, and 4 (see Fig. 1.4) are displayed. The cube-roots of the vector magnitudes are shown in addition to the internal scaling used in the rendering program (MATLAB) to keep the vectors visible while pointing out differences in magnitudes. Cube-root scaled vector magnitudes can be accurately compared within a figure, but not between figures, because the program's internal scaling differs between figures. These maps are projections on the $x-z$ axis and do not display vertical (y) vector information.

At some frequencies and scan locations the approximate intensity magnitude increased in measurement planes farther away from the shear layer, likely due to ground reflections. In general,

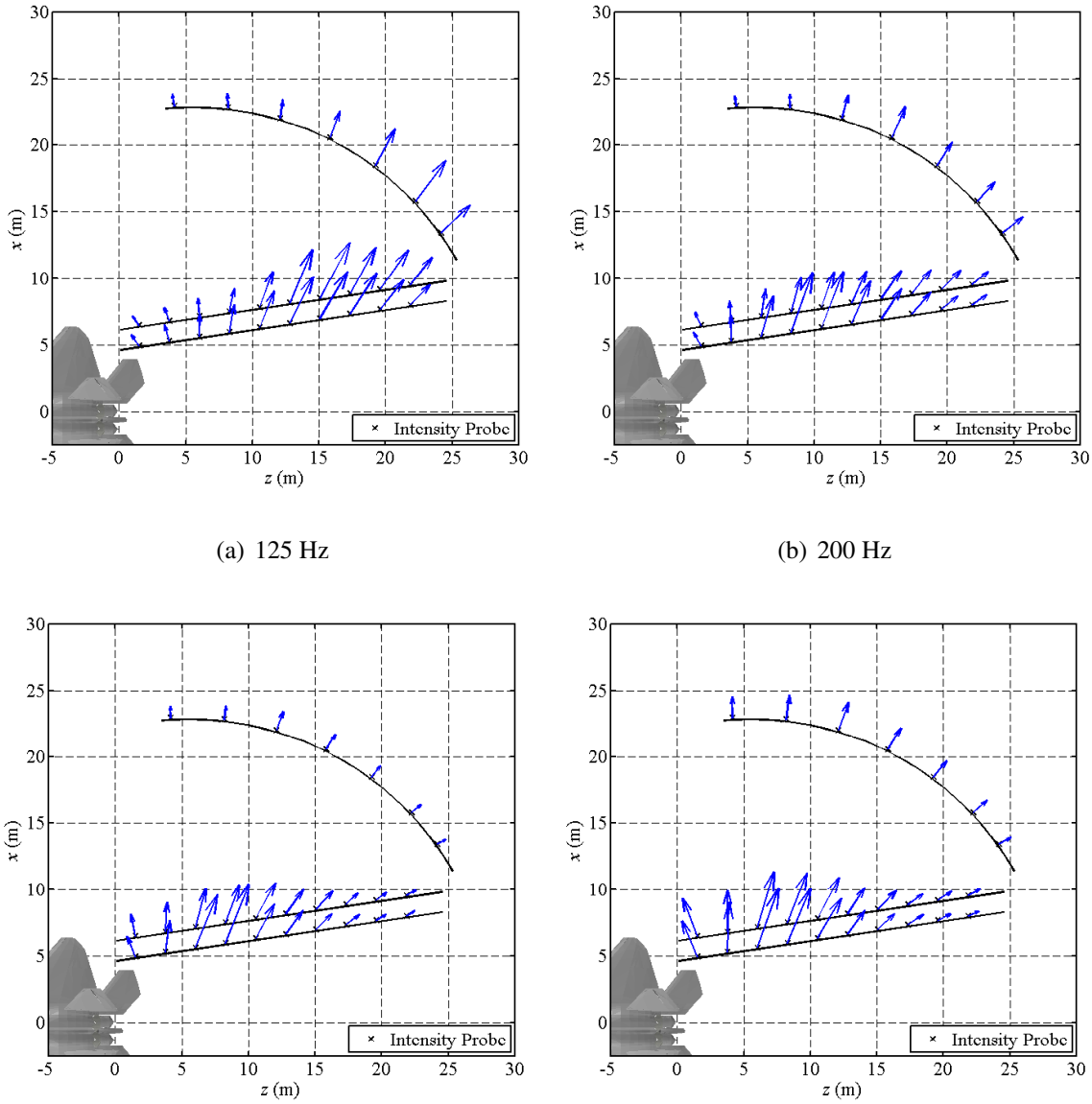

(a) 125 Hz

(b) 200 Hz

(c) 500 Hz

(d) 800 Hz

Figure 3.1 Intensity maps for measurement planes 1, 2, and 4 at (a) 125 Hz, (b) 200 Hz, (c) 500 Hz, and (d) 800 Hz, for afterburner engine condition. The nozzle of the active engine lies at the origin of the coordinate axes.

intensity magnitudes diminish with increasing distance from the source, since the energy being propagated outward must spread over a larger area. However, in areas where ground reflections

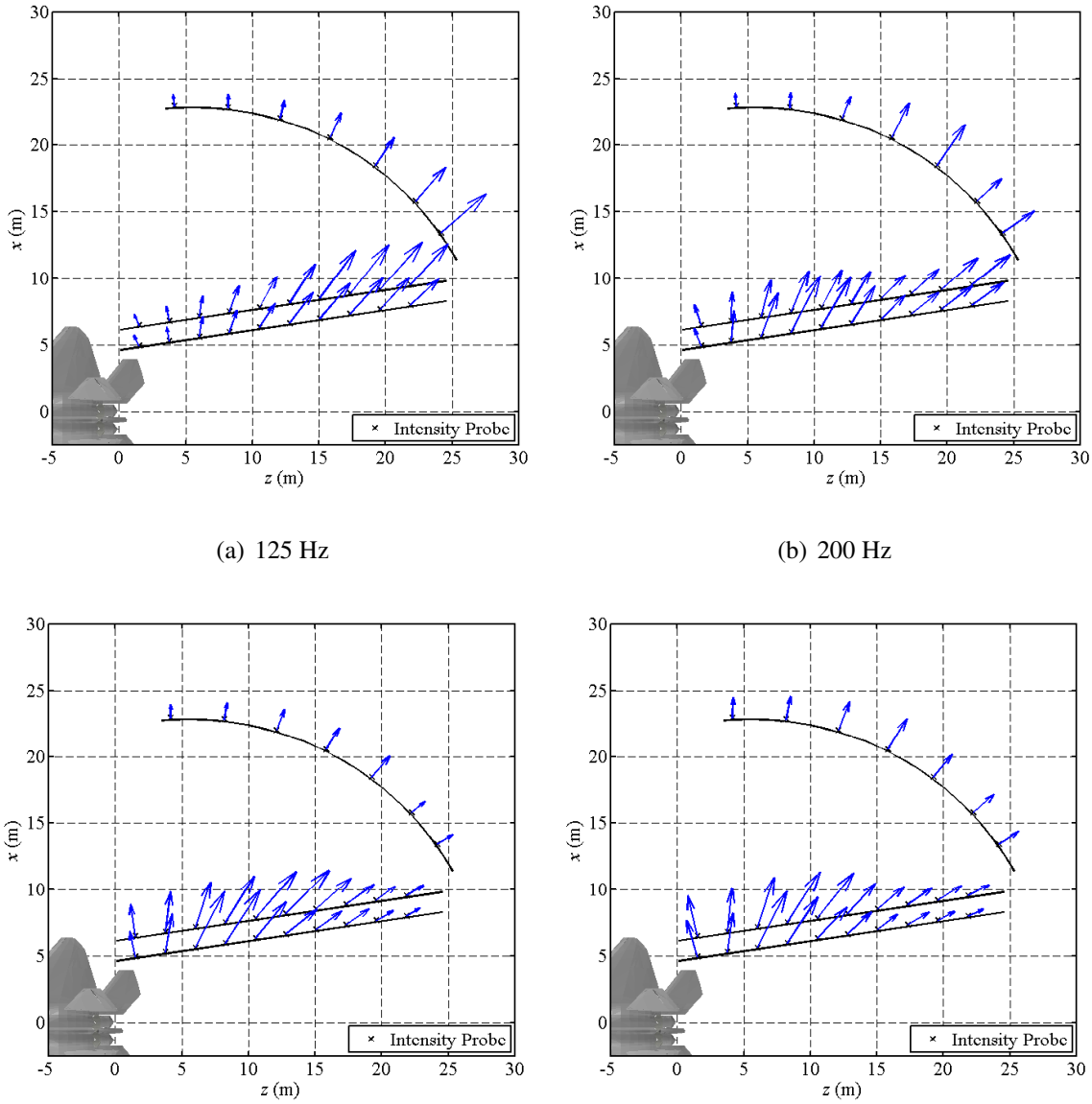

(a) 125 Hz

(b) 200 Hz

(c) 500 Hz

(d) 800 Hz

Figure 3.2 Intensity maps for measurement planes 1, 2, and 4 at (a) 125 Hz, (b) 200 Hz, (c) 500 Hz, and (d) 800 Hz, for military engine condition.

interfered constructively with the direct sound, the resulting pressure measurements and intensity approximations increased as opposed to measurements without ground reflections. For the maps of afterburner and military engine conditions, the effect is not as apparent as it is for intermediate

and idle conditions. However, in Fig. 3.1(a), for scans 6-10, (the half farther from the military jet), the vectors in measurement plane 2 exceed the magnitude of those in plane 1, a clear indication of interference. This is easier to see in Figs. 3.2(a), 3.2(c), and 3.3(a).

The effect of ground reflections is not easy to model or predict, but it is known to be a frequency- and location-specific influence [19]. Accounting precisely for ground reflections is outside the present scope of this thesis but is an important topic for future research.

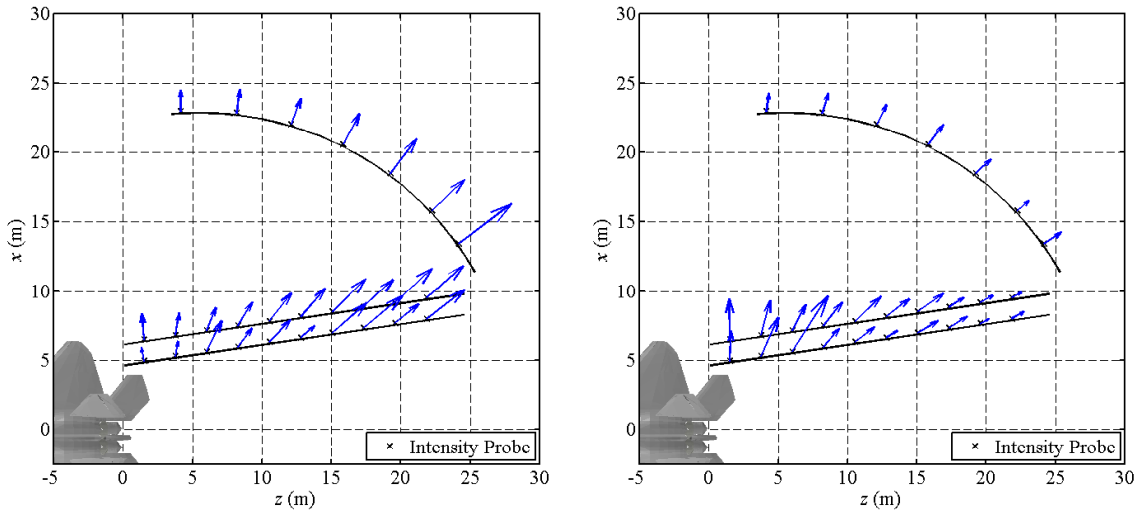

(a) 125 Hz (b) 500 Hz

Figure 3.3 Intensity maps for measurement planes 1, 2, and 4 at (a) 125 Hz, and (b) 500 Hz, for intermediate engine condition.

Variations in the engine run-up testing environment also impacted the results of these maps; especially evident is the inconsistent directionality of plane 1 vectors in Figs. 3.4(a) and 3.4(b) for idle engine conditions. For engine conditions besides afterburner and military, engine throttle consistency was subject to the human error of the F-22 pilot. A difference in engine output between scans affects the amount of energy flow emanating from farther downstream in the jet plume, affecting the intensity directionality as shown.

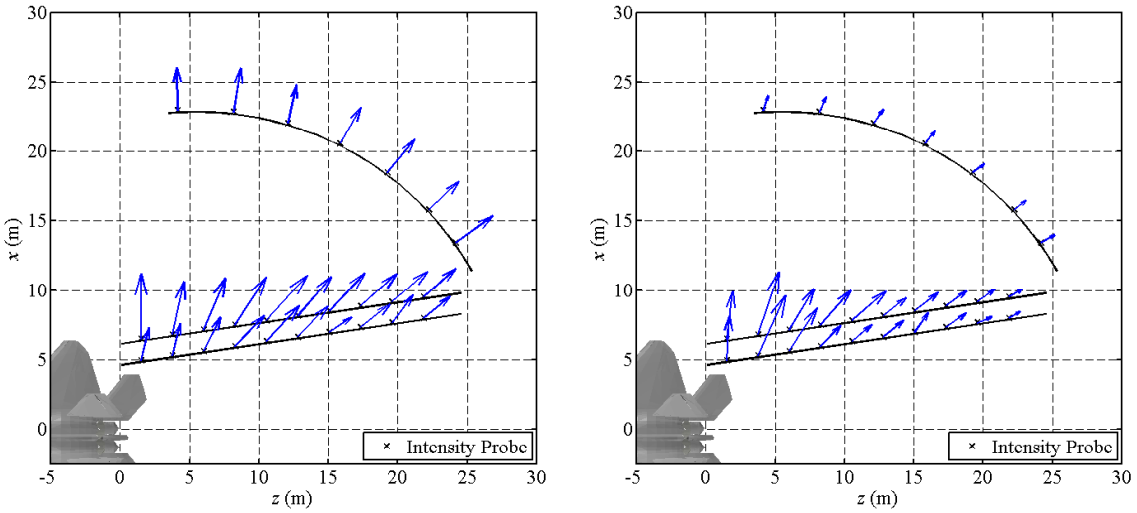

(a) 125 Hz (b) 500 Hz

Figure 3.4 Intensity maps for measurement planes 1, 2, and 4 at (a) 125 Hz, and (b) 500 Hz, for idle engine condition.

3.2 Source directionality

To compensate for the effects of ground reflections and run-up variation, the techniques detailed in Chapter 2 provided a generalized region of source directionality. The impact of ground reflections and run-up variation on intensity magnitudes between scans was lessened by taking the 3dB-down region into account. Figure 3.5 below summarizes the range of intensity vector directions contained in the 3dB-down regions, for one-third octave center band frequencies, military and afterburner conditions measured on plane 2 (see Fig. 1.3).

Though the directionalities fluctuate depending on frequency, there are a few overall trends that emerge. The general behavior of direction vs frequency is similar between the two engine conditions, however the intensity vector directions at military power center around 120°, whereas for afterburner they center around 110°. For both, the directionality moves closer to the 90° (towards the sideline) direction with increasing frequencies. Additionally, the 3dB-down region is

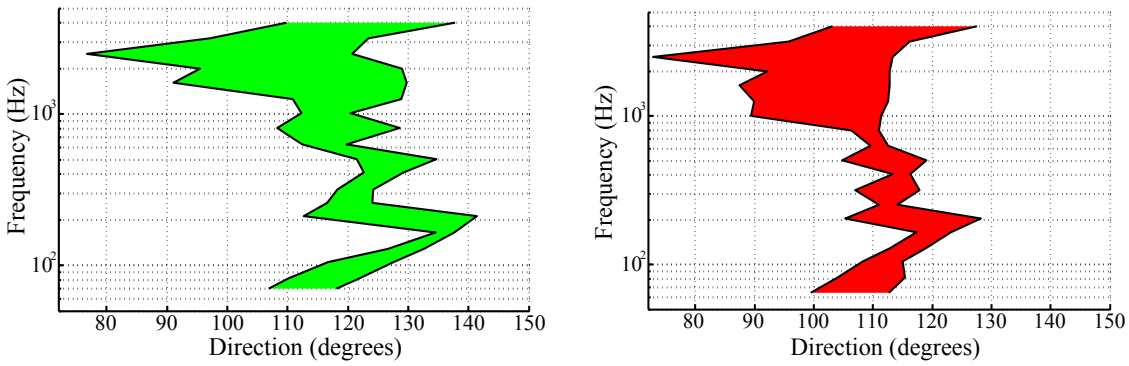

(a) Military

(b) Afterburner

Figure 3.5 Range of acoustic intensity directions contained in the 3dB-down regions for each one-third-octave band from measurement plane 2, for military (a) and afterburner (b) engine conditions. Note that 0° corresponds to the engine inlet.

very directional at the low-frequencies, but the width of included directions broadens significantly above about 600 Hz. This broader directionality indicates that the source behaves more like an omnidirectional monopole at higher frequencies.

3.3 Source location

The vectors contained in the 3dB-down region were also traced back to the jet centerline to give an approximation of the extended source location. Figure 3.6 below shows the source location vs frequency for the same set of measurements and conditions as in Fig. 3.5.

Again, the main difference between the source locations for military and afterburner conditions is an offset of the results. For all frequencies, the source location for military condition is about 1 m farther upstream. However, both conditions show the same trend, in that the source region contracts dramatically and moves upstream with higher frequency. For military condition, the contraction is especially pronounced; after about 250 Hz the source region stays under 1 m in width and at 4 kHz moves to within 2 m from the nozzle exit.

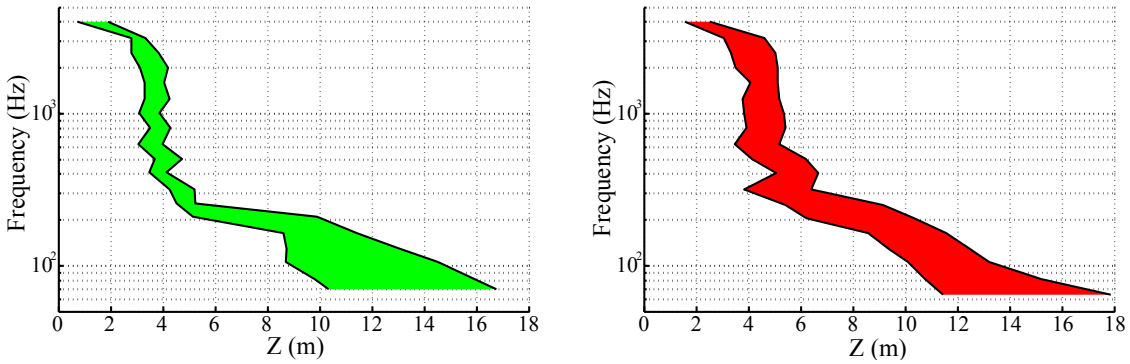

(a) Military (b) Afterburner

Figure 3.6 Source region location predictions based off of the 3dB-down regions for each one-third-octave band from measurement plane 2, for (a) military and (b) afterburner engine conditions. The intensity vectors in Fig. 3.5 are traced to the jet centerline. $Z = 0$ m corresponds to the jet nozzle exit.

3.4 Discussion

As shown by the intensity maps, the region of maximum energy flow moves upstream as frequency increases. A comparison of intensity data at high engine power along measurement planes 1 and 2 in Figs. 3.2(a) and 3.2(d) shows how the region shifts dramatically over this 25 m range. This movement is also seen in plane 4, however, because of the geometry of this plane, (the measurements on the arc are closer to the approximate shear layer with increasing z), the magnitudes are skewed to be higher for larger distance along the z-axis. For lower-throttle engine conditions, (see Figs. 3.4(a) and 3.4(b)), the shift is not as apparent because for these conditions the jet plume did not extend as far into the measurement region.

When tracing the vectors in the 3dB-down region back to the jet centerline, the shift in source location is especially pronounced. Both the intensity maps (Figs. 3.1(a)-3.4(b)) and directionality (Fig.3.5) in the 3dB-down regions also show how the direction of the energy flow points farther towards the sideline and less aft as frequency increases.

These trends are consistent with other methods and theories which predict that large-scale turbulent structures located farther downstream in the jet plume are a greater source of low-frequency noise than the small-scale structures, which produce more high-frequency content, that form closer to the jet nozzle. The apparent source location shifts as shown because of the contributions of both source mechanisms.

3.5 Results comparisons

To give these intensity results some context within the larger project involving the F-22 measurements and within the jet noise community, I present some select end results of other analysis methods here, and discuss how they compare to the intensity results. In general, these other methods agree in the general frequency trend in that the source location contracts and moves upstream with increasing frequency, but there is some disagreement about the exact location of the source region.

3.5.1 Equivalent source model

An equivalent source model (ESM) has been developed which matched the measured F-22 data against calculated data simulated from a simpler model of the noise source [20]. The source was modeled as two series of closely-spaced monopoles placed along the jet axis, one phase correlated and one uncorrelated. The amplitudes of the monopoles were weighted based on their location in order to most closely match the measured data through a Bayesian optimization algorithm. To compare the source predictions of ESM with those found using the intensity methodology, I chose to consider the location-based amplitudes of the correlated array, because the correlated distribution had higher amplitudes overall relative to the uncorrelated array.

Figure 3.7 displays the amplitudes of the correlated distribution along the jet centerline. For

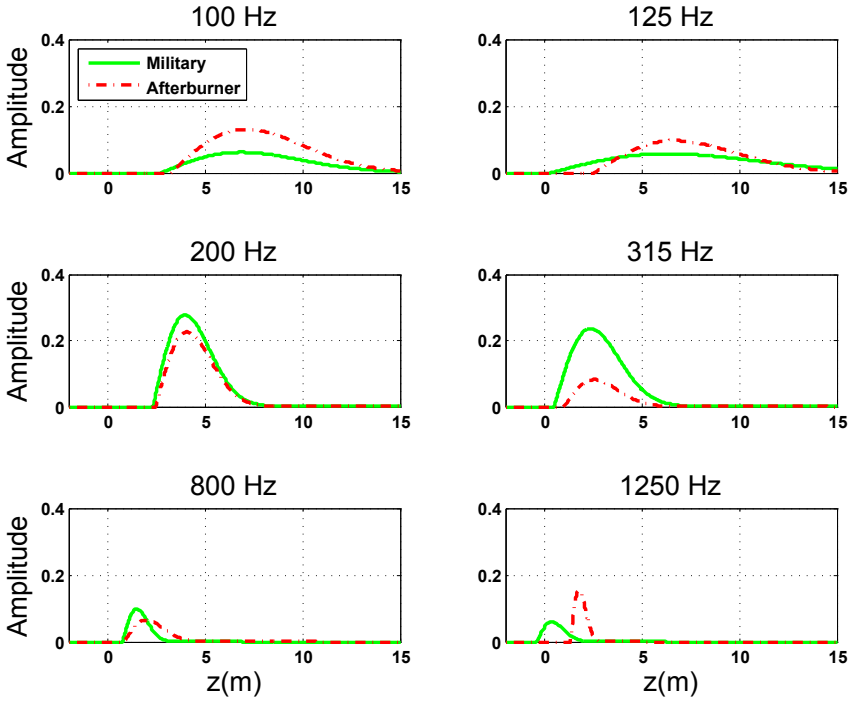

Figure 3.7 ESM distribution amplitude as a function of distance along the jet centerline, for military and afterburner conditions (from Hart [20]). The shape of the amplitude curves should be compared, rather than the absolute magnitudes.

these frequencies, these are the optimized distributions which most closely match the measured F-22 data. The shape of the amplitude weightings should be considered, rather than the magnitude of the amplitudes (because the ESM attempted to match the shape of measured data, and was shifted after the reconstruction to match the magnitude of the measured data). For both engine conditions shown, the source location distribution contracts in width and moves upstream (closer to $z = 0$) with increasing frequency – the same trend predicted by the intensity analysis. However, comparing Fig. 3.7 with Figs. 3.6(a)-3.6(b) reveals that ESM predicts a source farther upstream at all frequencies. At 100 Hz, ESM predicts a distribution centered around 7 m downstream, whereas intensity vectors point to a source around 13-14 m. For 315 Hz, the ESM distribution centers around 3 m downstream, and intensity points to 5-6 m.

3.5.2 Near-field acoustical holography

The measured data from the F-22 measurements were also processed and near-field acoustical holography (NAH) applied to project predicted acoustic quantities at locations outside of the measurement [21]. A process called Partial Field Decomposition broke up the measured pressure field into partial fields, which NAH then expanded to the reconstruction location. By expanding the fields to a reconstruction location close to the assumed source, along the shear layer, NAH predicted the source distributions as a function of frequency.

The source locations predicted by NAH (see Fig. 3.8) follow the same frequency trend, and agree more closely to the intensity predictions than those made by ESM. At 500 Hz, the top 3 dB of the NAH reconstruction is located between 2-5 m downstream, matching the intensity prediction narrowly centered at 4 m. The NAH reconstruction high-amplitude region travels to 4-6 m at 250 Hz and to 5-7 m at 200 Hz, which overlaps with the intensity predictions. At lower frequencies around 100 Hz, the NAH reconstruction has high-amplitude contributions much farther downstream, around 14-22 m, and still has some contribution closer to the jet nozzle at 3-7 m. The

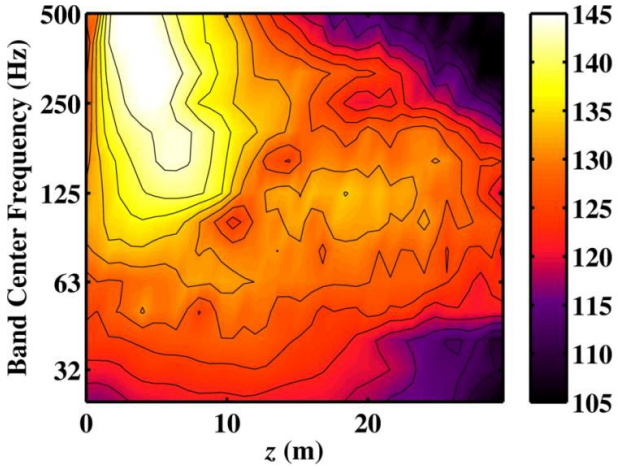

Figure 3.8 NAH source distributions reconstructed along the shear layer for military engine conditions at one-third-octave band center frequencies (from Wall [21]). The color scale is in dB, and the contour lines occur at 3 dB intervals.

source location prediction using the intensity method, however, does not provide such detail in the source location structure, but does point to a source at 9-14 m, in between the two regions found by NAH.

3.5.3 Beamforming

Beamforming is a processing technique that uses phase information to find the signal coming from the source in a given direction. By scanning over a desired region, beamforming can reconstruct the source amplitudes and locations. The problem of locating the jet source location region was also studied using beamforming techniques applied to a jet rig, with maximum mach number about 2, placed within a 65 foot radius anechoic dome [2]. Lee and Bridges took measurements of the jet rig using 16 microphones on the floor, parallel with the jet centerline. Their beamforming results for a heated jet flow are presented in Fig. 3.9.

Although the jet used was not full-scale, the beamforming source location reconstruction exhibits the same trend in frequency; the source region contracts somewhat and moves upstream with

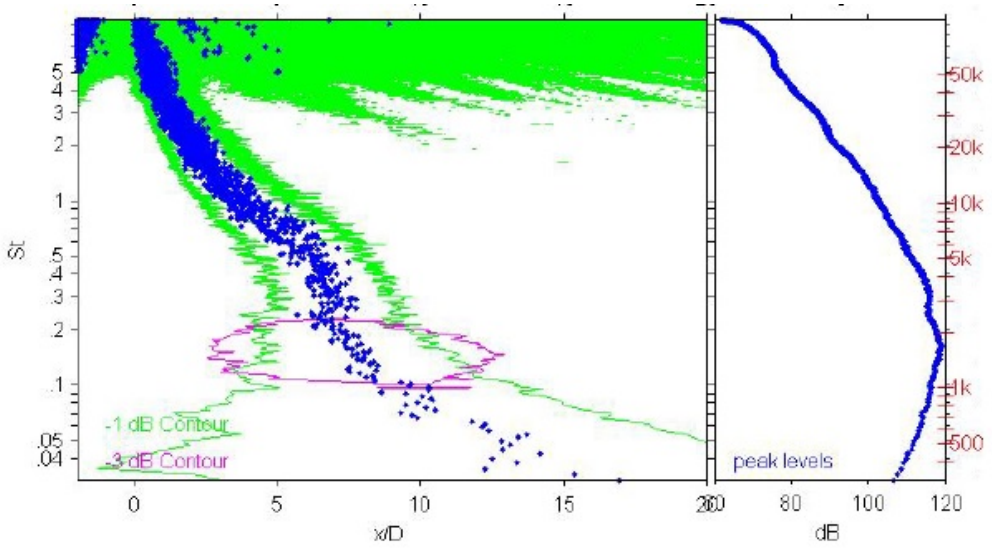

Figure 3.9 Beamforming source location results of a heated jet (from Lee and Bridges [2]). Peak source locations (left plot) and levels (right plot) are indicated by the blue dots. The Strouhal numbers on the left vertical axis correspond to the frequency scale on the right-most vertical axis. The horizontal axis is scaled by the jet nozzle diameter of 2 in. The most useful information is found below 50kHz.

increasing frequency. This shift occurs much more gradually in frequency, as opposed to the rapid source location change from 100 Hz to 300 Hz in the F-22 data.

Chapter 4

Conclusion

The results of the intensity analysis performed on the F-22 acoustical data is summarized as follows:

1. Intensity maps can be made to track frequency-specific sound energy flows emanating from a full-scale military jet using a tetrahedral intensity probe.

2. 3dB-down region directionalities show that noise propagates in a direction less aft at higher frequencies.

3. 3dB-down regions include a much broader directionality at frequencies higher than about 600 Hz, meaning that the source behaves more like an omnidirectional monopole at these frequencies.

4. Ray-tracing from 3dB-down regions show that the general source location region contracts and moves upstream with increasing frequency, with a rapid shift between 100 and 300 Hz.

The intensity study performed herein is the first application of this method to noise from military aircraft and leaves much room for future work. Some important considerations to be dealt with include construction of a model to account for ground reflection, and a more rigorous method

of source characterization. Future studies would also benefit from a more dense array of intensity probe locations, so that the spatially-varying effect of ground reflections could be more easily seen and accounted for, and so that a ray-traced source location region could be more precise.

As I hope has been demonstrated in this thesis, intensity measurements hold great potential for increasing our understanding of the acoustic source regions in military aircraft noise.

Bibliography

[1] S. R. Ventakesh, D. R. Poak, and S. Narayana, "Beamforming algorithm for distributed source localization and its application to jet noise," AIAA J. **41,** 1238–1246 (2003).

[2] J. B. Sang Soo Lee, "Phased-array measurements of single flow hot jets," AIAA J. 2842 (2005).

[3] A. T. Wall, K. L. Gee, M. D. Gardner, T. B. Neilsen, and M. M. James, "Near-field acoustical holography applied to high-performance jet aircraft noise," Proc. Mtgs. Acoust. 9 (2011).

[4] A. T. Wall, K. L. Gee, T. B. Neilsen, D. W. Krueger, M. M. James, S. D. Sommerfeldt, and J. D. Blotter, "Full-scale jet noise characterization using scan-based acoustical holography," AIAA J. pp. 2012–2081 (2012).

[5] J. Morgan, T. B. Neilsen, K. L. Gee, A. T. Wall, and M. M. James, "Simple-source model of high-power jet aircraft noise," Noise Control Eng. J. **60,** 435–449 (2012).

[6] P. N. Shah, H. Vold, and M. Yang, "Reconstruction of far-field noise using multireference acoustical holography measurements of high-speed jets," AIAA Paper pp. 2011–2772 (2012).

[7] R. E. K. J. Laufer, R. Schlinker, "Experiments on supersonic jet noise," AIAA Journal **14,** 489–497 (1976).

[8] S. M. Jaeger and C. S. Allen, "Two-dimensional sound intensity analysis of jet noise," AIAA Paper (1993).

[9] K. L. Gee, J. H. Giraud, J. D. Blotter, and S. D. Sommerfeldt, "Near-field vector intensity measurements of a small solid rocket motor," J. Acoust. Soc. Am. **128,** EL69–EL74 (2010).

[10] K. L. Gee, J. H. Giraud, J. D. Blotter, and S. D. Sommerfeldt, "Energy-based acoustical measurements of rocket noise," AIAA Paper (2009).

[11] M. M. James and K. L. Gee, "Advanced acoustic measurement system for rocket noise source characterization," Proc. Internoise 12 (2012).

[12] A. T. Wall, K. L. Gee, M. M. James, K. A. Bradley, S. A. McInerny, and T. B. Neilsen, "Near-field noise measurements of a high-power jet aircraft," Noise Control Eng. J. **60,** 421–434 (2012).

[13] M. M. James and K. L. Gee, "Aircraft jet plume source noise measurement system," Sound Vib. **44,** 14–17 (2010).

[14] F. Jacobsen, "Sound intensity and its measurement and applications," Acoustic Technology, Technical University of Denmark (2006).

[15] J.-C. Pascal and J.-F. Li, "A systematic method to obtain 3D finite-difference formulations for acoustic intensity and other energy quantities," J. Sound Vib. **310,** 1093–1111 (2008).

[16] D. C. Thomas, "Theory and Estimation of Acoustic Intensity and Energy Density," Brigham Young University, Master's thesis (2008).

[17] T. Rossing, *Springer Handbook of Acoustics*, *Springer handbooks* (Springer, 2007).

[18] J. H. Giraud, "Experimental Analysis of Energy-Based Acoustic Arrays for Measurement of Rocket Noise Fields," Brigham Young University, Master's thesis (2013).

[19] D. McLaughlin, C.-W. Kuo, and D. Papamoschou, "Experiments on the Effect of Ground Reflections on Supersonic Jet Noise," AIAA Paper 22 (2008).

[20] D. M. Hart, "Bayesian optimization of an equivalent source model for military jet aircraft," Brigham Young University, Senior thesis (2013).

[21] A. T. Wall, "The characterization of military aircraft jet noise using near-field acoustical holography methods," Brigham Young University, Ph.D. thesis (2013).

Index